ChemComm

Check for updates

Polymorphism-dependent room-temperature phosphorescence of a persulfurated benzene

Simone d'Agostino, [iD] *[a] Andrea Vitale, [iD] [a] Yashraj Kapadiya, [iD] [b] Marc Gingras, [iD] *[b] Fabrizia Negri, [iD] *[a] Paola Ceroni [iD] [a] and Andrea Fermi [iD] *[a]

Persulfurated benzenes are efficient room-temperature phosphorescent materials whose emission strongly depends on solid-state organization. We report two polymorphs (I and II) of A6-iPr exhibiting distinct RTP colors arising from different molecular conformations in the crystal lattice. Quantum chemical calculations reveal how conformation and intermolecular interactions govern the nature of the emissive triplet state.

Room-temperature phosphorescence (RTP) from metal-free, purely organic crystalline materials is a rare but highly desirable photophysical phenomenon.[1–4] Such materials are attractive for a plethora of potential applications in optoelectronics, sensing, and bioimaging because of their structural versatility, environmental compatibility, and potential for low-cost processing.[5–10] This is unlike costly, rare and metal-containing complexes, where strong spin–orbit coupling (SOC) enables efficient intersystem crossing. However, all-organic systems face intrinsic challenges due to the weakness of SOC in lighter elements.[11]

To overcome the typical limitations of organic crystalline RTP materials, one strategy involves the formation of co-crystals with heavy-atom-containing co-formers, such as perhalogenated species, which enhance spin–orbit coupling through the external heavy-atom effect.[12–17] An alternative strategy relies on the exploitation of the so-called Aggregation-Induced Emission (AIE)[18–21] as a mean to induce phosphorescence in in all-organic crystals, since slight differences in molecular packing with diverse supramolecular π–π interactions or hydrogen bonding networks can profoundly alter intersystem crossing efficiency and triplet exciton stabilization.[22–25]
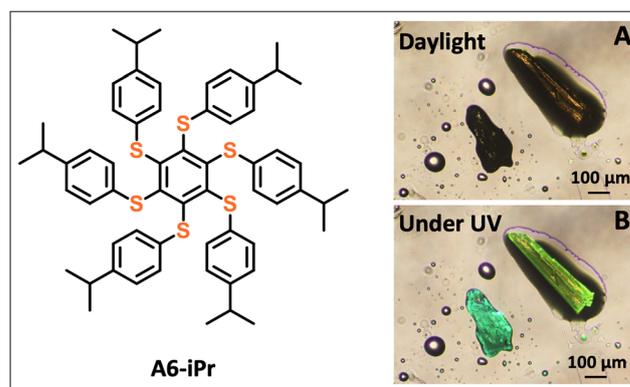
Among crystalline molecular materials that exhibit luminescence, arylthio-substituted persulfurated benzenes represent a promising family of solid-state room temperature phosphorescent (RTP) emitters.[26–29] Recently, we disclosed that a persulfurated derivative bearing six extended biphenyl arms act as a chemosensor by modulating its RTP behavior depending on the reversible uptake and release of solvent molecules,[30] which induces conformational and crystal packing changes.[31]

As part of our ongoing research in this area, we report here our findings about the polymorphic behavior of a member of this class of compounds, namely 1,2,3,4,5,6-hexakis((4-isopropyl-phenyl)thio)benzene, referred hereafter as **A6-iPr** (Scheme 1). The characteristic feature of **A6-iPr** is the presence of six bulky 4-isopropylphenyl groups, which were introduced because they potentially allow variable molecular conformations,[32,33] thereby promoting crystal polymorphism. In this context, we demonstrate that **A6-iPr** exists in two polymorphic forms, with distinct emissive behaviors. The crystals were analysed by combining several methods: powder and single-crystal X-ray diffraction (SC-XRD), microcalorimetric analysis, combined with luminescence spectroscopy and computational methods.

[a] Dipartimento di Chimica "Giacomo Ciamician", Alma Mater Studiorum–Università di Bologna, via Pietro Gobetti 85 –, 40129 Bologna, Italy.
E-mail: simone.dagostino2@unibo.it, fabrizia.negri@unibo.it, andrea.fermi@unibo.it

[b] Aix Marseille Univ., CNRS, CINAM, Marseille, France.
E-mail: marc.gingras@univ-amu.fr

Scheme 1 Molecular structure of 1,2,3,4,5,6-hexakis((4-isopropyl-phenyl)thio)benzene (**A6-iPr**) and optical images of single-crystal specimens of its two polymorphic forms with different emissions, photographed under daylight (A) and under 365 nm LED illumination (B).

Compound **A6-iPr** (Scheme 1) was prepared *via* an established protocol that allows complete nucleophilic aromatic substitutions onto perhalogenobenzene molecule, in the presence of an excess of arylthiol and a base (*e.g.*, K_2CO_3, *t*-BuOK, or NaH) in polar aprotic solvents, such as DMF (see SI for details).[34,35] Recrystallization of **A6-iPr** from the slow evaporation of a toluene solution afforded two distinct yellow crystals that upon UV excitation exhibited different emission colors, namely green or yellow emission, as depicted in Scheme 1. This prompted us to elucidate their respective crystal structures *via* SC-XRD and other methods.

Structural analysis of the bright-green emissive crystals revealed that the compound crystallizes in the trigonal $R\bar{3}$ space group (see Table S1 for details). As shown in Fig. 1, the six peripheral (4-isopropyl)phenylthio groups are arranged in an *ababab* pattern, where *a* and *b* denote substituents positioned above and below the plane of the central benzene ring, respectively. In contrast, structural analysis of the yellow emissive **A6-iPr** crystals revealed that the compound crystallises in the monoclinic $P2_1/c$ space group (see Table S1 for details). In this case, six (4-isopropyl)phenylthio substituents on the benzene core adopt an *aaabbb* arrangement, giving rise to a chair-like conformation (Fig. 2B and movie in the SI). Since no solvent is present in either case, the two crystals represent a true conformational polymorphic system. Therefore, we designate as Form I and Form II the green or yellow emissive crystals, respectively.

The polymorphs show subtle conformational differences in the persulfurated benzene core, which is essentially planar in Form I and slightly distorted in Form II, as indicated by small SC–CS torsion angles ($3.7°$ and $2.1–8.2°$, respectively). These conformational differences therefore primarily affect the crystal packing and intermolecular contacts rather than the intrinsic geometry of the central cores (see Fig. S4). In Form I, the molecules stack into perfectly aligned columns, whereas in Form II, they adopt a slipped columnar arrangement (see Fig. 2). It is worth noting that in **A6-iPr** Form I, the alternating *ababab* conformation of the substituents around the central benzene core prevents intermolecular π–π interactions by keeping the central cores at 8.9 Å from each other. On the contrary, in Form II the chair-like *aaabbb* conformation leaves the central cores partly free to interact with each other and, as a result, they are located
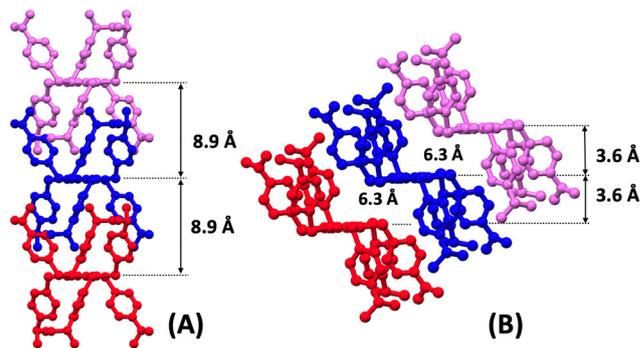

Fig. 2 Molecular stacking arrangements within crystalline **A6-iPr** Form I (A) and Form II (B). The distances represent the interplanar and centroid-to-centroid distances between the persulfurated benzene cores as detected in crystalline **A6-iPr** Forms I and II (H_{CH} atoms not shown for clarity).

at closer distances (6.3 Å). Additionally, Hirshfeld surface and fingerprint plot analyses using Crystal Explorer[36,37] reveals a weak C–H···S interaction $[H_{CH}···S = 2.83(3)\text{ Å}]$ between stacked molecules in Form II. In contrast, no significant intermolecular interactions are observed in Form I (see Fig. S5 and S6). To evaluate the magnitude of intermolecular interactions in the two polymorphs, intermolecular interaction energies (IIEs)[38] analyses. In both cases, IIEs calculations (see supporting information) indicate that the strongest interactions occur within the columnar stackings shown in Fig. 2, with total energies of -137.6 and $-122.4\text{ kJ mol}^{-1}$ for Form I and Form II, respectively. As expected, the IIEs are dominated by the dispersion component of the total energy (Fig. S9 and Table S2). Consequently, cohesion within both polymorphs arises primarily from dispersion forces, and molecular packing is mainly governed by shape complementarity.[39] Powder XRD analyses were performed to verify the correspondence between the crystalline structures and the phases present in the polycrystalline samples. As expected, the sample obtained from toluene contained both polymorphic forms, whereas the one produced directly from synthesis (using DMF as solvent), or from recrystallization from acetone and chloroform contained exclusively Form I (see Fig. S7). In contrast, pure polycrystalline Form II could be isolated by a thermal method.

Thermogravimetric analysis (TGA) of a polycrystalline sample of **A6-iPr** Form I showed no weight loss up to approximately 270 °C, indicating good thermal stability (Fig. S10). Differential scanning calorimetry (DSC) was employed to investigate possible phase transitions and to establish a relationship between the two forms. **A6-iPr** Form I exhibited an endothermic peak at approximately 180 °C ($\Delta H_f = 28.5\text{ kJ mol}^{-1}$) on heating, consistent with melting, while no thermal events were detected during cooling. In the subsequent heating cycle, an exothermic peak appeared at around 88 °C ($\Delta H_c = -18.3\text{ kJ mol}^{-1}$), corresponding to a recrystallization process, followed by an endothermic peak at approximately 155 °C ($\Delta H_f = 18.7\text{ kJ mol}^{-1}$), consistent with a melting process (see Fig. S11). These results suggest that upon melting and cooling, **A6-iPr** Form I can be converted into an amorphous material which, upon further heating, recrystallizes
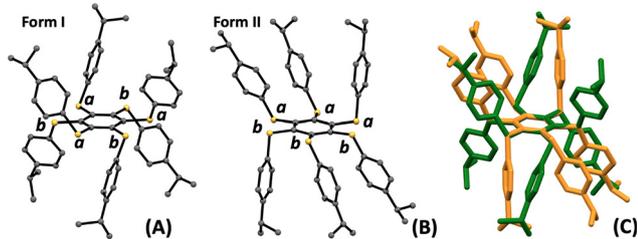

Fig. 1 Molecular structures of **A6-iPr** Form I (A) and II (B), as determined from SC-XRD. Letters in lowercase indicate the orientations of the peripheral (4-isopropyl)phenylthio substituents with respect to the central benzene unit (a: above; b: below). (C) Overlay diagram showing the conformational differences between the two forms (H_{CH} omitted for clarity).

into a different polymorph, likely **A6-iPr** Form II, melting at lower temperature.

To gain further insight, these structural transformations associated with such transitions were monitored by variable-temperature powder XRD (see Fig. S8). The results showed a good agreement with the DSC analyses, *i.e.*, Form I melts at about 180 °C and, when cooled to RT, remains in an amorphous state which upon further heating recrystallizes into Form II. Moreover, this process enabled the bulk preparation of a polycrystalline sample for the second polymorph (see Fig. S7 and S8). The differences in melting points and ΔH_f support the assignment of Form II as a metastable phase, while Form I corresponds to the more stable one. In a non-polar solvent (*e.g.* toluene) multiple conformers may coexist and become kinetically trapped during nucleation, leading to the formation of distinct crystal nuclei and concomitant polymorphs. In contrast, crystallization from polar solvents yields the stable polymorph, likely suppressing the formation of conformers required for nucleation of the metastable form.

The photophysical properties were first evaluated in solution at RT and key data are reported in Table 1. The absorption spectrum of **A6-iPr** in CH_2Cl_2 is similar to those observed for other hexakis-(arylthio)benzenes analogues,[27] with a broad lower-energy lying absorption band showing a maximum at 326 nm ($\varepsilon = 19\,200$ M^{-1} cm^{-1}; see Fig. S10). In analogy, the emission properties of **A6-iPr** in diluted solutions match those displayed by its congeners,[29] with negligible emission at RT (either in air-equilibrated or degassed solutions) and an intense green phosphorescence in rigid matrices at 77 K (CH_2Cl_2: CH_3OH, 1:1, v/v), with emission quantum yield around 0.5 and a lifetime in the order of 10^{-3} s. No fluorescence has been observed from the solids at RT, nor in diluted conditions at 77 K.

As anticipated, the photophysical behavior is peculiar for each polymorph of **A6-iPr** in the solid-state (see Fig. 1, 3 and Table 1): conversion from Form I to II leads to a red-shift of the emission spectrum, to a decrease in the emission lifetime, and to a significant quenching of the luminescence quantum yield (see computational discussion below). This behavior is consistent with that observed for other persulfurated derivatives exhibiting conformational flexibility.[28,30]

Luminescence analysis of the polymorphs at low temperatures substantially shows unchanged emission spectra for both forms in the solid state, whereas the lifetime increases up to 6.4 ms in the case of Form II (see Table S3), likely as a
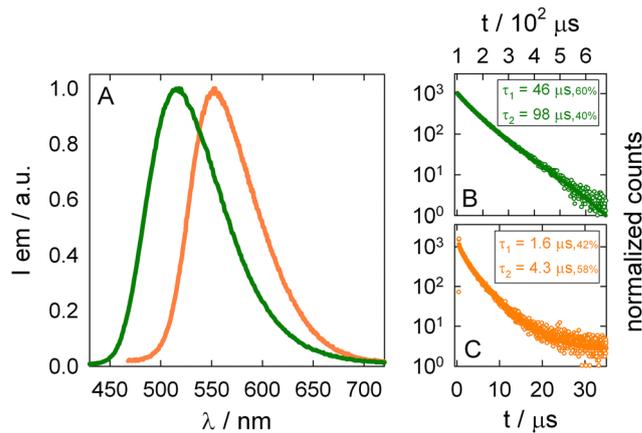

Fig. 3 (A) emission spectra recorded for solid state **A6-iPr** at RT (green line: Form I; orange line: Form II; λ_{ex} = 360 nm). (B) and (C) Emission decays recorded from the two polymorphs under the same experimental conditions are also shown for Form I and Form II with green and orange dots, respectively, together with biexponential fitting functions. λ_{ex} = 405 nm; λ_{em} = 510 nm for Form I; λ_{em} = 560 nm for Form II.

consequence of the decrease of the non-radiative constant. In addition, as highlighted for similar compounds,[29] amorphous phases of **A6-iPr** are showing intense emission only at low temperature, while it is negligible at RT: this observation indicates that the crystallinity of the material in both Form I and II is required in order to achieve significant emission at RT. The emission properties of the two forms were computationally investigated by DFT and TDDFT calculations. Ground-state geometry optimizations in the gas phase and in the crystal, reveal pronounced differences for the *ababab* conformer. In the gas phase, this conformer relaxes to a folded structure, whereas such folding is hindered in the crystalline environment (see Fig. S16 and S17). In contrast, the *aaabbb* conformer does not adopt a folded geometry in the gas phase, resulting in similar structures in both gas and crystalline phases (see Fig. S20 and S21). The orbital character of the T_1 state is also influenced by the folded or unfolded geometry of the *ababab* conformer in Form I. Despite a pronounced quinoidal distortion for both situations, (Fig. S18 and S19), in the gas phase the dominant $\pi\pi^*$ character of the T_1 state induces a substantial out-of-plane distortion of the central benzene core. Such distortions are commonly associated with low-energy emission and reduced quantum yield due to enhanced intersystem crossing with the

Table 1 Photophysical data for **A6-iPr** in solution and in the solid state

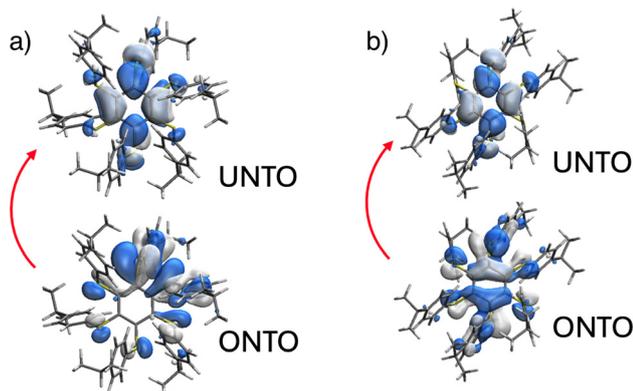| Entry	Solution						
	Absorption	Emission, 77 K					
	CH_2Cl_2, RT	CH_2Cl_2:CH_3OH (1:1, v/v)			Solid state emission, RT		
	λ (nm)/ε (M^{-1} cm^{-1})	λ_{max} (nm)	τ (ms)	Φ	λ_{max} (nm)	τ (μs)	Φ
A6-iPr	326/19 200	502	3.3–8.7[a]	0.5	—	—	—
A6-iPr Form I	—	—	—	—	518	46–98[a]	0.4
A6-iPr Form II	—	—	—	—	554	1.6–4.3[a]	<0.1

[a] Biexponential fitting.

Fig. 4 Natural Transition Orbital (NTO) analysis (QM/MM calculations) showing the excitation from the occupied (ONTO) to the unoccupied (UNTO) of **A6-iPr** Form I (a) and Form II (b).

S_0 state.[29] Consistent with this interpretation, the calculated gas-phase emission energy is as low as 1.70 eV (Table S5). By contrast, in the crystal the optimized T_1 geometry displays predominantly $n\pi^*$ character (Fig. 4A and Fig. S26). As established in previous studies,[29] such $n\pi^*$ states are typically associated with higher emission energies and enhanced luminescence efficiency due to reduced spin–orbit coupling, both of which are consistent with the experimental observations. Accordingly, the computed emission energy in the crystalline phase is 2.68 eV (Table S5). The calculations indicate less pronounced differences between the gas phase and crystalline environments for the lowest triplet state of the *aaabbb* conformer (Fig. S22 and S23). In both phases, the T_1 state retains a mixed $n\pi^*/\pi\pi^*$ character (see Fig. 4B and Fig. S26) and features a quinoidal central benzene ring that remains essentially planar in the excited state). The computed emission energy amounts to 2.35 eV in the gas phase and decreases to 2.28 eV in the crystal, yielding a value in close agreement with the experimental data.

Although enhanced excitonic interactions could, in principle, account for the experimentally observed red shift in Form II, TDDFT calculations on dimer and trimer aggregates of the *aaabbb* conformer do not support this hypothesis, revealing only a modest change in the $S_0 \rightarrow T_1$ excitation energy (2.97 eV *versus* 2.96 eV; Table S6). In short, the crystal packing constraints in Form I play a crucial role in favoring unfolded *ababab* conformations with a lowest $n\pi^*$ triplet state. The mixed $n\pi^*/\pi\pi^*$ character of the lowest triplet state in Form II is responsible for the reduced emission energy.

Our investigations revealed the existence and interconversion of two distinct crystalline forms of **A6-iPr**. Although they exhibit similar appearances, the photophysical properties displayed by Forms I and II are markedly different, reflecting the conformations adopted in the solid state: phosphorescence emission switches from green to yellow, respectively. Experimental data are corroborated by quantum-chemical calculations. Overall, this work highlights the crucial influence of polymorphism on the emissive behavior of fully organic phosphorescent materials.

Conflicts of interest

There are no conflicts to declare.

Data availability

Acknowledgements

Notes and references

1 S. d'Agostino, F. Spinelli, P. Taddei, B. Ventura and F. Grepioni, *Cryst. Growth Des.*, 2019, **19**, 336–346.
2 A. A. Dar and A. A. Malik, *J. Mater. Chem. C*, 2024, **12**, 9888–9913.
3 X. Shen, W. Wu and C. Yang, *Molecules*, 2024, **29**, 3236.
4 M. Stanitska, D. Volyniuk, B. Minaev, H. Agren and J. V. Grazulevicius, *J. Mater. Chem. C*, 2024, **12**, 2662–2698.
5 H. Xiang, J. Cheng, X. Ma, X. Zhou and J. J. Chruma, *Chem. Soc. Rev.*, 2013, **42**, 6128.
6 S. Ito, *CrystEngComm*, 2022, **24**, 1112–1126.
7 M. Ji and X. Ma, *Ind. Chem. Mater.*, 2023, **1**, 582–594.
8 S. Ito, *Advances in Organic Crystal Chemistry*, Springer Nature Singapore, Singapore, 2025, pp. 121–142.
9 L. Yang, L.-H. Xiong and X. He, *Chem. Biomed. Imaging*, 2025, **3**, 499–521.
10 X. Yang, M. Zhang, B. Tang, L. Wang, B. Yang, L. Li, P. Naumov and H. Zhang, *J. Am. Chem. Soc.*, 2025, **147**, 22961–22971.

11 J. Li, Q. Yao, L. Wu, Z. Hu, B. Gao, X. Wan and Q. Liu, *Nat. Commun.*, 2022, **13**, 919.

12 H. Y. Gao, Q. J. Shen, X. R. Zhao, X. Q. Yan, X. Pang and W. J. Jin, *J. Mater. Chem.*, 2012, **22**, 5336.

13 S. d'Agostino, F. Grepioni, D. Braga and B. Ventura, *Cryst. Growth Des.*, 2015, **15**, 2039–2045.

14 L. Li, W. X. Wu, Z. F. Liu and W. J. Jin, *New J. Chem.*, 2018, **42**, 10633–10641.

15 Y. Xia, Y. Du, Q. Xiang and M. G. Humphrey, *New J. Chem.*, 2021, **45**, 4930–4933.

16 A. Azzali, S. d'Agostino, M. Capacci, F. Spinelli, B. Ventura and F. Grepioni, *CrystEngComm*, 2022, **24**, 5748–5756.

17 C. Zhang, X. Jiang, C. Wang, Z. Liu, B. Xu and W. Tian, *Smart Mol.*, 2025, **3**, e20240054.

18 M. Baroncini, G. Bergamini and P. Ceroni, *Chem. Commun.*, 2017, **53**, 2081–2093.

19 J. Yang, M. Fang and Z. Li, *Aggregate*, 2020, **1**, 6–18.

20 D. Galicia-Badillo, J. L. Belmonte-Vázquez, M. Rodríguez, B. Rodríguez-Molina and M. C. García-González, *ACS Omega*, 2024, **9**, 38015–38022.

21 Y. Zhang, B. Bai, G. A. Alfani, Z. Zhao and B. Z. Tang, *J. Mater. Chem. C*, 2025, **13**, 20806–20824.

22 M. Hayduk, S. Riebe and J. Voskuhl, *Chem. – Eur. J.*, 2018, **24**, 12221–12230.

23 J. You, X. Zhang, Q. Nan, K. Jin, J. Zhang, Y. Wang, C. Yin, Z. Yang and J. Zhang, *Nat. Commun.*, 2023, **14**, 4163.

24 D. Zhong, S. Liu, L. Yue, Z. Feng, H. Wang, P. Yang, B. Su, X. Yang, Y. Sun and G. Zhou, *Chem. Sci.*, 2024, **15**, 9112–9119.

25 A. Fermi, *ChemPhotoChem*, 2025, **9**, e202400404.

26 G. Bergamini, A. Fermi, C. Botta, U. Giovanella, S. Di Motta, F. Negri, R. Peresutti, M. Gingras and P. Ceroni, *J. Mater. Chem. C*, 2013, **1**, 2717–2724.

27 A. Fermi, G. Bergamini, R. Peresutti, E. Marchi, M. Roy, P. Ceroni and M. Gingras, *Dyes Pigm.*, 2014, **110**, 113–122.

28 H. Wu, G. V. Baryshnikov, A. Kuklin, B. F. Minaev, B. Wu, L. Gu, L. Zhu, H. Ågren and Y. Zhao, *ACS Appl. Mater. Interfaces*, 2021, **13**, 1314–1322.

29 A. Fermi, S. d'Agostino, Y. Dai, F. Brunetti, F. Negri, M. Gingras and P. Ceroni, *Chem. – Eur. J.*, 2024, **30**, e202401768.

30 A. Fermi, S. Gahlot, E. Jorand, S. d'Agostino, Y. Dai, F. Negri, C. Moustrou, M. Gingras and P. Ceroni, *J. Am. Chem. Soc.*, 2025, **147**, 32309–32314.

31 S. E. Wright, J. C. Cole and A. J. Cruz-Cabeza, *Cryst. Growth Des.*, 2021, **21**, 6924–6936.

32 D. D. MacNicol and D. R. Wilson, *J. Chem. Soc., Chem. Commun.*, 1976, 494–495.

33 A. D. U. Hardy, D. D. MacNicol, S. Swanson and D. R. Wilson, *J. Chem. Soc., Perkin Trans. 2*, 1980, 999.

34 L. Testaferri, M. Tingoli and M. Tiecco, *J. Org. Chem.*, 1980, **45**, 4376–4380.

35 M. Gingras, J. Raimundo and Y. M. Chabre, *Angew. Chem. Int. Ed.*, 2006, **45**, 1686–1712.

36 M. A. Spackman and D. Jayatilaka, *CrystEngComm*, 2009, **11**, 19–32.

37 P. R. Spackman, M. J. Turner, J. J. McKinnon, S. K. Wolff, D. J. Grimwood, D. Jayatilaka and M. A. Spackman, *J. Appl. Crystallogr.*, 2021, **54**, 1006–1011.

38 C. F. Mackenzie, P. R. Spackman, D. Jayatilaka and M. A. Spackman, *IUCrJ*, 2017, **4**, 575–587.

39 D. Braga, S. d'Agostino and F. Grepioni, *Organometallics*, 2012, **31**, 1688–1695.

40 (*a*) CCDC 2522427: Experimental Crystal Structure Determination, 2026, DOI: 10.5517/ccdc.csd.cc2qnsmt; (*b*) CCDC 2522428: Experimental Crystal Structure Determination, 2026, DOI: 10.5517/ccdc.csd.cc2qnsnv; (*c*) CCDC 2522429: Experimental Crystal Structure Determination, 2026, DOI: 10.5517/ccdc.csd.cc2qnspw; (*d*) CCDC 2522430: Experimental Crystal Structure Determination, 2026, DOI: 10.5517/ccdc.csd.cc2qnsqx.